

Dual oxygen and temperature luminescence sensor based on artificial intelligence

FRANCESCA VENTURINI^{1,2,*}, UMBERTO MICHELUCCI², AND MICHAEL BAUMGARTNER¹

¹Institute of Applied Mathematics and Physics, Zurich University of Applied Sciences, Technikumstrasse 9, 8401 Winterthur, Switzerland

²TOELT LLC; Birchlenstr. 25, 8600 Dübendorf, Switzerland

*Corresponding author: francesca.venturini@zhaw.ch

Compiled February 23, 2020

A well-known optical approach to measure oxygen partial pressure is the quenching of luminescence by the oxygen molecules. Sensors based on this principle typically rely on approximate empirical models to parametrise the dependence of the sensing quantity on influencing factors, like the temperature. In this work, we propose a new artificial intelligence neural network approach which allows the extraction of both the oxygen concentration and the temperature using one single dye molecule and measuring a single quantity, namely the decay time. The results demonstrate that firstly, using neural networks it is possible to extract both the oxygen concentration and the temperature from the measurement of one single quantity and using one single indicator; secondly, that the use of the proposed neural networks allow more accurate and stable predictions for both the parameters. Furthermore, the proposed artificial intelligence approach is not limited to oxygen and temperature sensing, but can be applied to luminescence of multiple indicators, whenever the underlying mathematical model is not known or too complex to derive the desired quantities from a single measurement.

© 2020 Optical Society of America under the terms of the [OSA Open Access Publishing Agreement](#)

<http://dx.doi.org/10.1364/optica.XX.XXXXXX>

1. INTRODUCTION

The simultaneous determination of multiple parameters can be very advantageous in many sensor applications, for example, when an in-situ or remote acquisition is required. If the measured parameters are interdependent or show cross-interference, their simultaneous determination becomes a necessity. Optical luminescence sensing has the advantage of enabling multiple sensing since the same optical elements, like optical fiber and detector, can be used, therefore allowing a compact and easy sensor design. The typical approaches are based on either the use of a single luminescence indicator (luminophore), whose luminescence is sensitive to more than one parameters or the use of several luminophores, one for each parameter, embedded in a substrate and placed in close physical proximity [1–6]. To be able to determine each parameter separately it is usually necessary to determine more than one optical property (e.g., absorption spectrum, emission spectrum, luminescence intensity, decay time)

or to use special detection schemes to take advantage of the differences of one optical property of the used luminophores [4, 7].

The problem of dual sensing is particularly relevant in applications which involve oxygen sensing. The determination of oxygen partial pressure is of great interest in numerous fields, like medicine, biotechnology, environmental monitoring, or chemistry since oxygen plays an important role in many processes [4, 8]. One of the most used optical measuring approaches uses the effect of the dynamical quenching of luminescence by the oxygen molecules. The measuring principle is based on the measurement of the luminescence of a specific luminophore, whose intensity and decay time are reduced due to collisions with molecular oxygen [9].

Sensors based on this principle must rely on empirical models to parametrize the dependence of the measured sensing quantity (ie.g., luminescence intensity or decay time) on influencing factors of the environment where the indicator is placed. Among

these, the parameter with the strongest influence is temperature, since both the luminescence and the quenching phenomena are strongly temperature dependent. Therefore, in any optical oxygen sensor the temperature must be continuously monitored, most frequently with a separate sensor, and used to correct the calculated oxygen concentration. This task can be difficult in a practical implementation and may be a major source of error in sensors based on luminescence sensing.

In this work we propose and demonstrate a revolutionary approach based on artificial intelligence to determine both the oxygen concentration and the temperature using one single indicator and measuring a single quantity, namely the decay time. The method is based on a multi-task learning (MTL) neural networks. This type of architectures are characterized by multiple branches of layers, that get their input from a common set of layers. Since the network can improve the model prediction performance by jointly learning correlated tasks [10–14], it was demonstrated to be flexible enough to be usable in multi-dimensional regressions [10].

large amount of data application to real data limitation and prospects.

IDEA

Pressure Sensitive Paint: any method requires correction due to the temperature dependence of the luminescence of the paint, for example non-oxygen quenched, temperature-dependent phosphor is added to the standard paint

2. METHODS

A. Luminescence Quenching for Oxygen Determination

Luminescence-based oxygen sensors usually consist of a dye molecule (luminophore) whose luminescence intensity and decay time decrease depending on the O_2 concentration. This reduction is due to collisions of the excited luminophore with molecular oxygen, which thus provide a radiationless deactivation process (collisional quenching). In the case of homogeneous media characterized by an intensity decay which is a single exponential, the decrease in intensity and lifetime are both described by the Stern-Volmer (SV) equation [9]

$$\frac{I_0}{I} = \frac{\tau_0}{\tau} = 1 + K_{SV} \cdot [O_2] \quad (1)$$

where I_0 and I , respectively, are the luminescence intensities in the absence and presence of oxygen, τ_0 and τ the decay times in the absence and presence of oxygen, K_{SV} the Stern-Volmer constant and $[O_2]$ indicates the oxygen concentration.

For practical applications, the luminophore needs to be embedded in a supporting substrate, frequently a polymer. As a result, the SV curve deviates from the linear behavior of equation (1). This deviation can be due, for example, to heterogeneities of the micro-environment of the luminescent indicator, or the presence of static quenching [4]. A scenario which describes this non-linear behavior involves the presence in the substrate of at two or more environments, in which the indicator is quenched at different rates [11, 12]. This multi-site model describes the SV curve as the sum of two or more

$$\frac{I_0}{I} = \left[\frac{f_i}{1 + K_{SV,i} \cdot [O_2]} \right]^{-1} \quad (2)$$

where I_0 and I , respectively, are the luminescence intensities in the absence and presence of oxygen, f_i 's are the fractions of the total emission for each component under unquenched conditions, $K_{SV,i}$'s are the associated effective Stern-Volmer constants,

and $[O_2]$ indicates the oxygen concentration. A simplification of this model is that one of the sites is not quenched and therefore the constant K_{SV2} is zero. Depending on the luminophore and on the substrate material, the proposed model may be even more complex [12–14].

Since in most industrial and commercial sensor applications, the decay time τ is frequently preferred to intensity measurement because of its higher reliability and robustness. The determination of the decay time is done most easily in the frequency domain by modulating the intensity of the excitation. As a result, the emitted luminescence is also modulated but shows a phase shift θ due to the finite lifetime of the excited state. This method, has the advantage of allowing very simple and low-cost realization and is widely used in commercial applications.

Although the multi-site model was introduced for luminescence intensities, it is frequently also used to describe the oxygen dependence of the decay times [12, 15]. Therefore, in the simplest case of a two-sites scenario, the model can be rewritten in terms of phase shift as [16]

$$\frac{\tan \theta(\omega, T, [O_2])}{\tan \theta_0(\omega, T)} = \left(\frac{f(\omega, T)}{1 + K_{SV1}(\omega, T) \cdot [O_2]} + \frac{1 - f(\omega, T)}{1 + K_{SV2}(\omega, T) \cdot [O_2]} \right)^{-1} \quad (3)$$

where θ_0 and θ , respectively, are the phase shifts in the absence and presence of oxygen, f and $1 - f$ are the fractions of the total emission for each component under unquenched conditions, K_{SV1} and K_{SV2} are the associated Stern-Volmer constants for each component, and $[O_2]$ indicates the oxygen concentration. It is to be noted that the quantities θ_0 , f , K_{SV1} , and K_{SV2} are all non-linearly temperature dependent and may result frequency dependent, an artifact of the approximation of the model. Finally, Eq. 3 needs to be inverted to determine $[O_2]$ from the measured quantity θ .

B. Experimental Setup

The optical setup used in this work for the luminescence measurements is shown schematically in Fig. 1. To be able to acquire a large number of data, both the software for the instrument control and for the data acquisition was written using LabVIEW by National Instruments. The acquisition procedure is described in detail in Sect. C.

The sample used for the characterization and test is a commercially available Pt-TFPP-based oxygen sensor spot (PSt3, PreSens Precision Sensing GmbH). To control the temperature of the samples, these were placed in good thermal contact with a copper plate, placed in a thermally insulated chamber. The temperature of this plate was adjusted using a Peltier element and stabilized with a temperature controller (PTC10, Stanford Research Systems). The thermally insulated chamber was connected to a self-made gas-mixing apparatus which enabled to vary the oxygen concentration between 0 % and 20 % vol O_2 by mixing nitrogen and dry air from two bottles. In the following, the concentration of oxygen will be given in % of the oxygen concentration of dry air and indicated with % air. This means, for example, that 20 % air corresponds to 4 % vol O_2 and 100 % air corresponds to 20 % vol O_2 . The absolute error on the oxygen concentration adjusted with the gas mixing device is estimated to be below 1 % air.

The excitation light was provided by a 405 nm LED (VAOL-5EUV0T4, VCC Visual Communications Company LLC), filtered

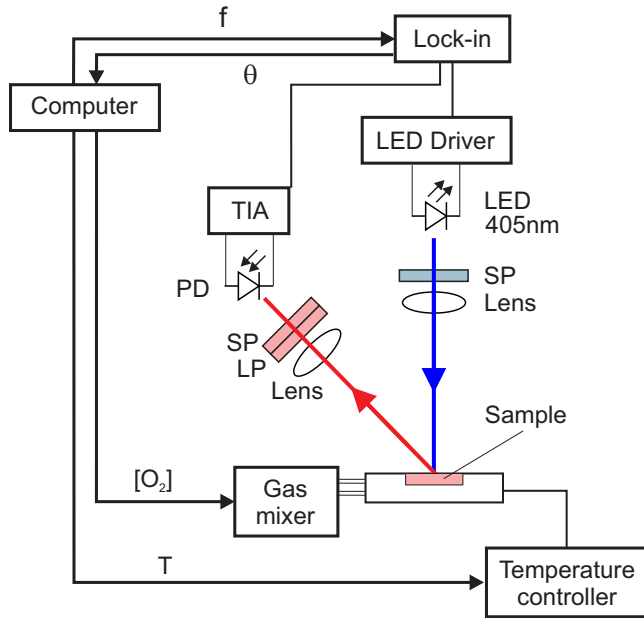


Fig. 1. Scheme of the optical experimental setup. Blue is the excitation, red the luminescence optical path. SP: short pass filter; LP: long pass filter PD: photodiode; TIA: trans-impedance amplifier.

by a an short pass (SP) filter with cut-off at 498 nm (Semrock 498 SP Bright Line HC short pass) and focused on the surface of the samples with a collimation lens (EO43987, Edmund Optics). The luminescence was focussed by a lens (G063020000, LINOS) and collected by a photodiode (SFH 213 Osram). To suppress stray light and light reflected by the sample surface, the emission channel was equipped with a long pass filter with cut-off at 594 nm (Semrock 594 LP Edge Basic long pass) and a short pass filter with cut-off at 682 nm (Semrock 682 SP Bright Line HC short pass). The driver for the LED and the trans-impedance amplifier (TIA) are self-made. For the frequency generation and the phase detection a two-phase lock-in amplifier (SR830, Stanford Research Inc.) was used.

C. Automated Data Acquisition

The series of measurements were carried out following the flow shown in Fig. 2. First the acquisition program fixed the temperature and concentration. Then the phase-shift was measured for varying the modulation frequency between 200 Hz and 15000 kHz. This measurement was repeated 20 times. Next, keeping the temperature fixed, the program changed the oxygen concentration and the entire frequency-loop was repeated. The oxygen concentration was varied between 0 % air and 100 % air in 5 % steps. Finally, the temperature is changed and then the oxygen and frequency loops where repeated. The temperature was varied between 5 °C and 45 °C in 5 °C steps. The total number of measurements is thus $50 \times 20 \times 21 \times 9 = 189000$ which required approximately 65 hours. This number of measurement was chosen as a compromise between maximizing the number of data for the training of the neural network and avoiding photodegradation, which naturally occurs when the sample is subjected to illumination. At the end of the session a minimal change in the phase shift was observed (QUANTIFY?)

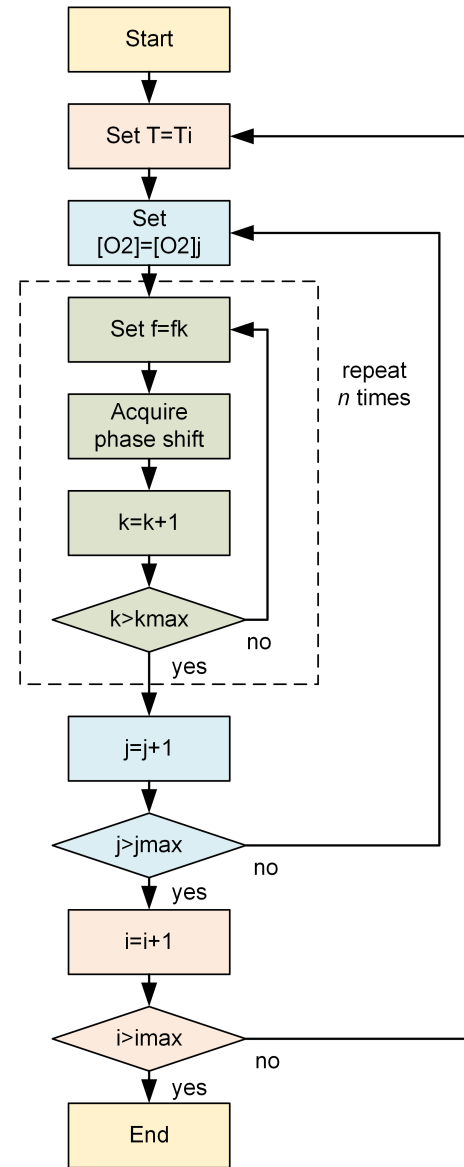


Fig. 2. Flow-chart of the automatic measurement process.

D. Artificial Neural Network Design

The artificial network used in this work has a multi-task-learning architecture and is depicted in Figure 3. It consists of three common hidden layers with 50 neurons each which generate as output a "shared representation". The name comes from the fact that the output of those layers is used to evaluate both $[O_2]$ and T . These are followed by three branches, two with each two additional "task-specific hidden layers" to predict respectively $[O_2]$ and T , and then one without additional layers to predict $[O_2]$ and T at the same time. The shared representation is the input of two "task-specific hidden layers", that learn how to predict $[O_2]$ and T better. This architecture uses the common hidden layers to find common features beneficial to each of the two tasks. During the training phase, learning to predict $[O_2]$ will influence the common hidden layers and therefore, the prediction of T , and vice-versa. The further task-specific hidden layers learn specific features to each output and therefore improve the prediction accuracy. The number of neurons of each task-specific hidden layer is 5.

As activation function the sigmoid activation functions was used for all the neurons. A common choice for the cost function in regression problems is the mean square error (MSE), which is defined as

$$MSE = \frac{1}{n} \sum_{j=1}^n \sum_{k=1}^d (y_k^{[j]} - \hat{y}_k^{[j]})^2 \quad (4)$$

where n is the number of observations in the input dataset; $y^{[j]} \in \mathbb{R}^d$ is the measured value of the desired quantity for the j^{th} observation (indicated as a superscript between square brackets), with $j = 1, \dots, n$; $\hat{y}^{[j]} \in \mathbb{R}^d$ is the output of the network, when evaluated on the j^{th} observation. Since there are multiple branches, a global cost function L needs to be defined as a linear combination of the task-specific cost functions with weights α_i will be minimized

$$L = \sum_{i=1}^{n_T} \alpha_i L_i. \quad (5)$$

The parameters α_i have to be determined during the hyperparameter tuning phase to optimize the network predictions. In this paper, being the cost function the MSE (Equation 4), the global cost function of Equation 5 is

$$L = \sum_{i=1}^{n_T} \alpha_i \frac{1}{n} \sum_{j=1}^n \sum_{k=1}^d (y_k^{[j]} - \hat{y}_k^{[j]})^2 \quad (6)$$

where n_T is the number of tasks; n is the number of observations in the input dataset; $y^{[j]} \in \mathbb{R}^d$ is the measured value of the desired quantity for observation j , with $j = 1, \dots, n$; $\hat{y}^{[j]} \in \mathbb{R}^d$ is the output of the network, when evaluated on the j^{th} observation. he global cost function weights used for the plots were $\alpha_1 = 0.3$, $\alpha_2 = 5$ and $\alpha_3 = 1$. Those values were chosen because they result in the lowest MAEs (see discussion in Section 3).

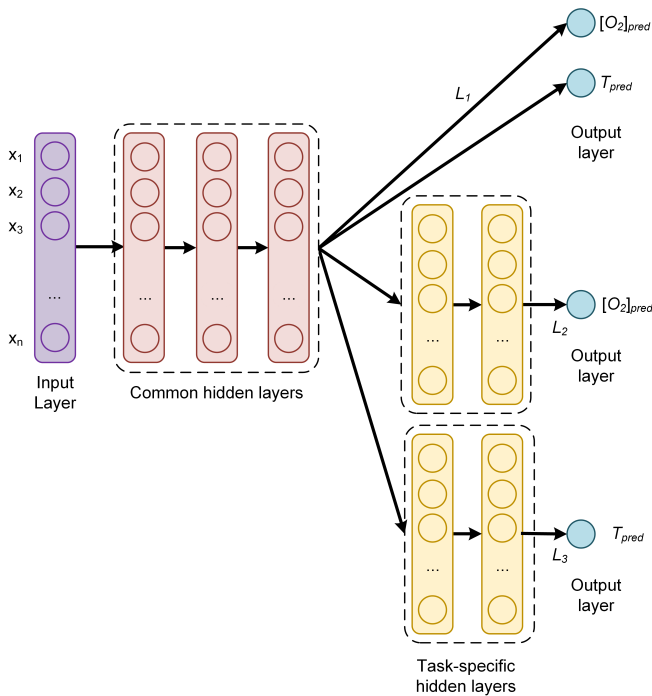


Fig. 3. Architecture of the multi-task learning architecture.

To minimize the cost function, the optimizer Adaptive Moment Estimation (Adam) [17, 18] was used. The training was

performed with a starting learning rate of 10^{-3} and using batch-learning, which means that the weights were updated only after the entire training dataset has been fed to the network. Batch-learning was chosen because of its stability and speed since it reduces the training time of a few orders of magnitude in comparison to, for example, stochastic gradient descent [18]. Therefore it makes experimenting with different networks a feasible endeavor. The implementation was performed using the TensorFlow library.

The metric used to compare results from different network models is the absolute error (AE) defined as the absolute value of the difference between the predicted and the expected value for a given observation. For the oxygen concentration of the j^{th} observation $[O_2]^{[j]}$ the AE is

$$AE_{[O_2]}^{[j]} = |[O_2]_{pred}^{[j]} - [O_2]_{meas}^{[j]}|. \quad (7)$$

The further quantity used to analyze the performance of the network is the mean absolute error (MAE), defined as the average of the absolute value of the difference between the predicted and the expected oxygen concentration or temperature. For example, for the oxygen prediction using the training dataset S_{train} , $MAE_{[O_2]}$ is defined as

$$MAE_{[O_2]}(S_{train}) = \frac{1}{|S_{train}|} \sum_{j \in S_{train}} |[O_2]_{pred}^{[j]} - [O_2]_{real}^{[j]}| \quad (8)$$

where $|S_{train}|$ is the size (or cardinality) of the training dataset. For example, in this work $|S_{train}|=20000$. The AE_T and MAE_T are similarly defined.

3. RESULTS AND DISCUSSION

A. Luminescence Experimental Results

As described in Section A, the phase-shift depends not only on the oxygen concentration, but also on the temperature and on the modulation frequency of the excitation light. This can be seen in the Figs. 4 to 6. Fig. 4 shows the measured phase shifts as a function of the oxygen concentration at a constant modulation frequency for increasing temperatures. For clarity, only selected temperatures are shown. The decrease in the phase shift with increasing concentration is the quenching of the luminescence described in Eq. 3. The effect of the temperature is to further decrease the phase shift but the effect depends on the concentration, being stronger at higher oxygen concentration. This temperature quenching is understandable since higher temperature...

For a given oxygen concentration the phase shift is strongly dependent from the modulation frequency, as it can be seen in Fig. 5. Again, the temperature quenching is visible and affects the phase shift differently depending on the modulation frequency.

The complementary to Fig. Fig. 5 is shown in Fig. 6, where the phase shift is shown a function of the modulation frequency for selected oxygen concentrations at a fixed temperature.

Comparing the curves shown above it is clear that, when measuring one single phase-shift or even a the phase-shift as a function of the modulation frequency is not possible to simultaneously determine both the oxygen concentration and the temperature from this set of data. To determine the oxygen concentration is mandatory to know the temperature. This is no longer the case with the artificial intelligence approach, as it will be shown in the next section.

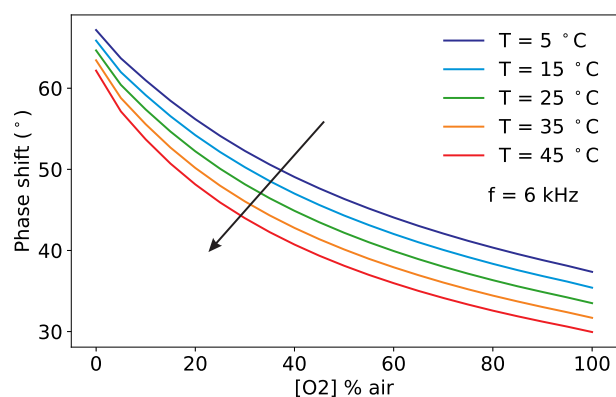


Fig. 4. Measured phase-shift as a function of the oxygen concentration, for selected temperatures at a fixed modulation frequency of 6 kHz. The arrow marks increasing temperatures.

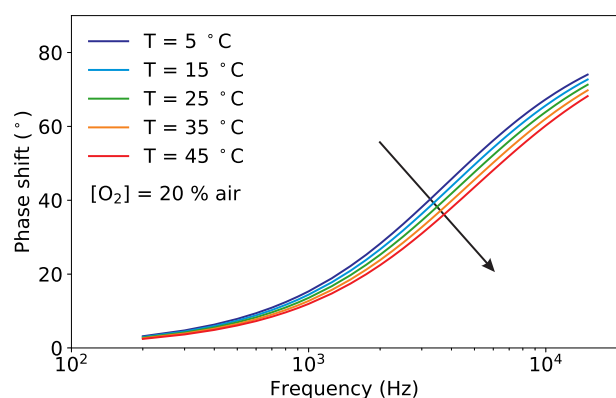


Fig. 5. Measured phase-shift for selected oxygen concentrations as a function of the modulation frequency at a fixed oxygen concentration $[O_2] = 20\%$ at selected temperatures.

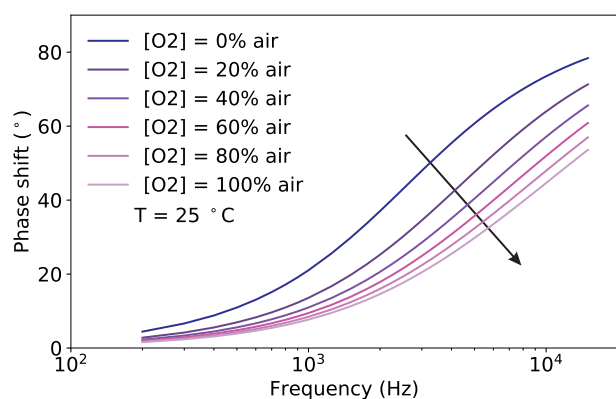


Fig. 6. Measured phase-shift for selected oxygen concentrations as a function of the modulation frequency at a fixed temperature $T = 25^\circ$.

B. Neural network performance

To analyze the performance of the network, a fundamental quantity is the prediction probability density?? distribution of the AEs since it carries information on the probability of the network to predict the expected value. for each parameter. For this reason the kernel density estimate (KDE) of the distributions of the AEs for both the oxygen concentration and the temperature was calculated. KDE is a non-parametric algorithm to estimate the probability density function of a random variable by inferring the population distribution based on a finite data sample [19]. ATTENZIONE COPIATO DA WIKIPEDIA In this work a Gaussian Kernel and a Scott bandwidth adaptive estimation [20] using the seaborn Python package [?] were used.

The results for $AE_{[O_2]}$ and AE_T for are shown in Figure 7.

Finally, the performance of the different neural networks is summarized in Table 1. Here the MAE as defined in Equation 8 for the oxygen concentration and the temperature prediction are listed.

Table 1. Summary of the performance for the three types of neural networks

Input	Epochs / Batch size	$MAE_{[O_2]}$	MAE_T
$\theta/90^\circ$	20'000 / 4000	xx % air	xx °C
$\theta/90^\circ$	20'000 / 32	xx% air	xx °C
$\theta/90^\circ$	100'000 / 32	xx % air	xx °C
θ/θ_0	20'000 / 32	xx % air	xx °C

plot theta/theta0 vs frequency for different T (O2 fix) and for different O2 (T fix) plot distribution of total AE

temperature can be presicted less well because phase shift depends less from T than from O2

Stability results

temperature cannot be predicted well without dividing for theta 0

4. CONCLUSIONS

DISCLOSURES

Disclosures. The authors declare no conflicts of interest.

REFERENCES

1. M. I. Stich, L. H. Fischer, and O. S. Wolfbeis, "Multiple fluorescent chemical sensing and imaging," *Chem. Soc. Rev.* **39**, 3102–3114 (2010).
2. S. M. Borisov, R. Seifner, and I. Klimant, "A novel planar optical sensor for simultaneous monitoring of oxygen, carbon dioxide, ph and temperature," *Anal. bioanalytical chemistry* **400**, 2463–2474 (2011).
3. T. Kameya, Y. Matsuda, Y. Egami, H. Yamaguchi, and T. Niimi, "Dual luminescent arrays sensor fabricated by inkjet-printing of pressure-and temperature-sensitive paints," *Sensors Actuators B: Chem.* **190**, 70–77 (2014).
4. X.-d. Wang and O. S. Wolfbeis, "Optical methods for sensing and imaging oxygen: materials, spectroscopies and applications," *Chem. Soc. Rev.* **43**, 3666–3761 (2014).
5. S. Santoro, A. Moro, C. Portugal, J. Crespo, I. Coelho, and J. Lima, "Development of oxygen and temperature

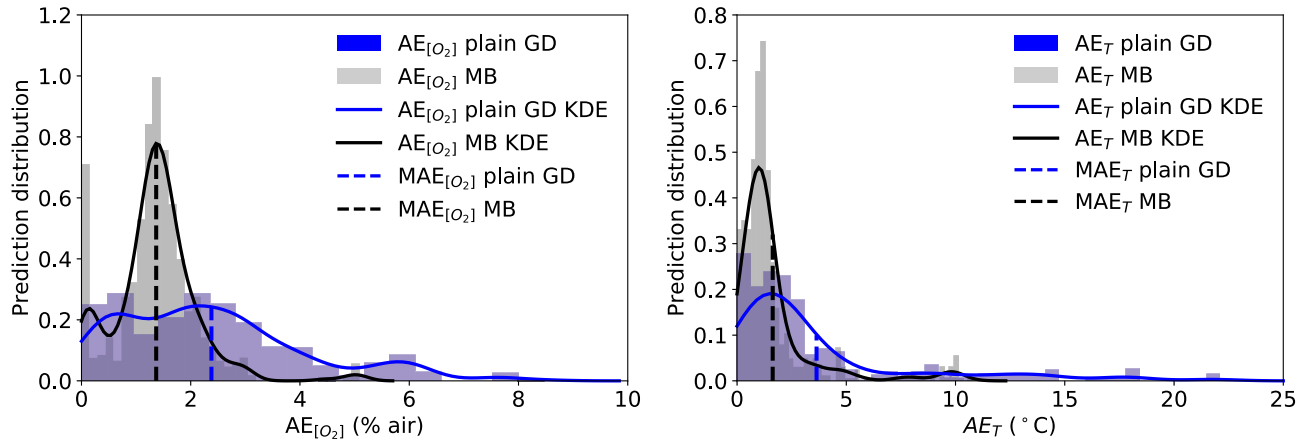


Fig. 7. Performance of the neural network for the oxygen (left plot) and for the temperature (right plot) predictions: Normalized prediction distribution histogram (columns) and kernel density estimate (KDE) of the distribution of the AEs (solid line) using plain gradient descent (GD) and using mini-batches (MB) with a batch size of 32. The corresponding MAE is also shown as a dashed line in each diagram.

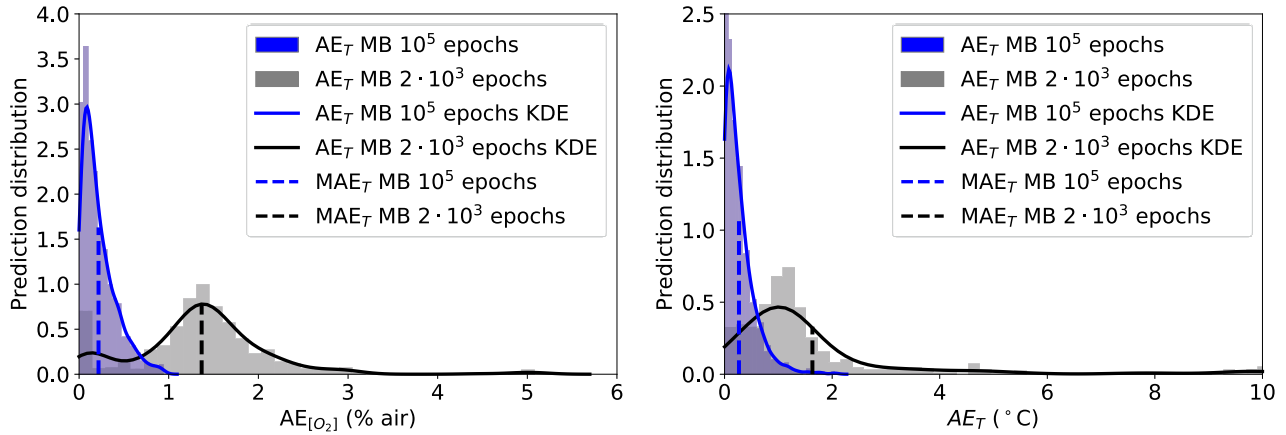


Fig. 8. Performance of the neural network for the oxygen (left plot) and for the temperature (right plot) predictions: Normalized prediction distribution histogram (columns) and kernel density estimate (KDE) of the distribution of the AEs (solid line) using plain gradient descent (GD) and using mini-batches (MB) with a batch size of 32. The corresponding MAE is also shown as a dashed line in each diagram.

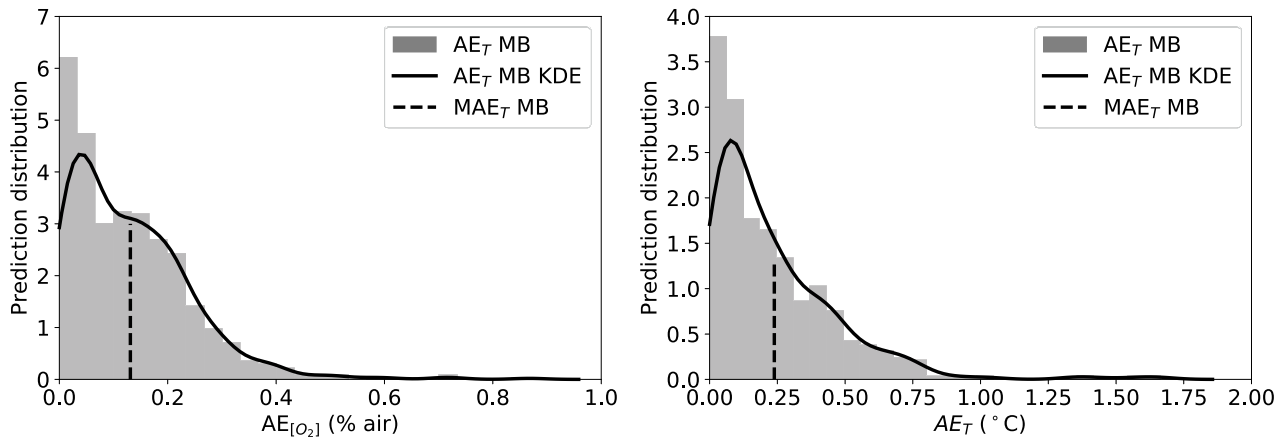


Fig. 9. Performance of the neural network for the oxygen (left plot) and for the temperature (right plot) predictions: Normalized prediction distribution histogram (columns) and kernel density estimate (KDE) of the distribution of the AEs (solid line) using plain gradient descent (GD) and using mini-batches (MB) with a batch size of 32. The corresponding MAE is also shown as a dashed line in each diagram.

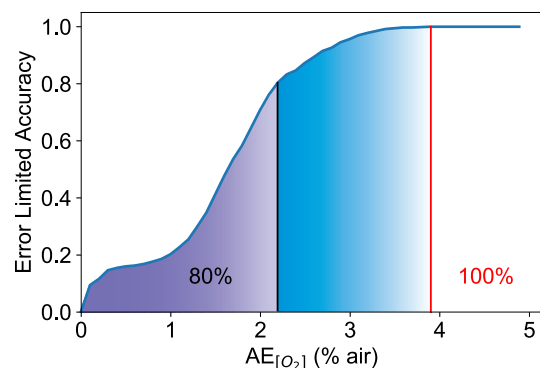


Fig. 10. Phase-shift at a fixed temperature $T = 25^\circ$ for selected oxygen concentrations as a function of the modulation frequency of the excitation light.

estimation," J. Am. Stat. Assoc. **91**, 1525–1534 (1996).

~

sensitive membranes using molecular probes as ratiometric sensor," J. Membr. Sci. **514**, 467–475 (2016).

6. S. Biring, A. S. Sadhu, and M. Deb, "An effective optical dual gas sensor for simultaneous detection of oxygen and ammonia," *Sensors*. **19**, 5124 (2019).
7. B. B. Collier and M. J. McShane, "Time-resolved measurements of luminescence," *J. Lumin.* **144**, 180–190 (2013).
8. D. B. Papkovsky and R. I. Dmitriev, "Biological detection by optical oxygen sensing," *Chem. Soc. Rev.* **42**, 8700–8732 (2013).
9. J. R. Lakowicz, *Principles of Fluorescence Spectroscopy*, 3rd ed. (Springer, New York, 2006).
10. U. Michelucci and F. Venturini, "Multi-task learning for multi-dimensional regression: application to luminescence sensing," *Appl. Sci.* **9**, 4748 (2019).
11. E. Carraway, J. Demas, B. DeGraff, and J. Bacon, "Photo-physics and photochemistry of oxygen sensors based on luminescent transition-metal complexes," *Anal. chemistry* **63**, 337–342 (1991).
12. J. N. Demas, B. DeGraff, and W. Xu, "Modeling of luminescence quenching-based sensors: comparison of multisite and nonlinear gas solubility models," *Anal. Chem.* **67**, 1377–1380 (1995).
13. P. Hartmann, M. J. Leiner, and M. E. Lippitsch, "Luminescence quenching behavior of an oxygen sensor based on a ru (ii) complex dissolved in polystyrene," *Anal. Chem.* **67**, 88–93 (1995).
14. A. Mills, "Response characteristics of optical sensors for oxygen: models based on a distribution in τ or k_q ," *Analyst*. **124**, 1301–1307 (1999).
15. M. Quaranta, S. M. Borisov, and I. Klimant, "Indicators for optical oxygen sensors," *Bioanal. reviews* **4**, 115–157 (2012).
16. U. Michelucci, M. Baumgartner, and F. Venturini, "Optical oxygen sensing with artificial intelligence," *Sensors* **19**, 777 (2019).
17. J. A. Kingma, D.P.; Ba, "Adam: A method for stochastic optimization. in proceedings of 3rd." In Proc. 3rd Int. Conf. on Learn. Represent. ICLR 2015 pp. 1–15 (2015).
18. U. Michelucci, *Applied Deep Learning - A Case-Based Approach to Understanding Deep Neural Networks* (APRESS Media, LLC, 2018).
19. T. Hastie, R. Tibshirani, and J. Friedman, *The elements of statistical learning: data mining, inference, and prediction* (Springer Science & Business Media, 2009).
20. S. R. Sain and D. W. Scott, "On locally adaptive density